Lawrence Berkeley National Laboratory
Recent Work

Title
THEORY OF ANGLE-RESOLVED PHOTOEMISSION EXTENDED FINE STRUCTURE

Permalink
https://escholarship.org/uc/item/4s81w03k

Authors
Barton, J.J.
Robey, S.W.
Shirley, D.A.

Publication Date
1985-12-01

Lawrence Berkeley Laboratory
UNIVERSITY OF CALIFORNIA

Materials & Molecular Research Division

THEORY OF ANGLE-RESOLVED PHOTOEMISSION
EXTENDED FINE STRUCTURE

J.J. Barton, S.W. Robey, and D.A. Shirley

December 1985

DISCLAIMER

Theory of Angle-Resolved Photoemission Extended Fine Structure

J.J. Barton, S.W. Robey, and D.A. Shirley

Materials and Molecular Research Division
Lawrence Berkeley Laboratory
and
Departments of Chemistry and Physics
University of California
Berkeley, California 94720

ABSTRACT

We present a theory for photoelectron scattering in the 100-1000 eV energy range designed to simulate experimental measurements of Angle-Resolved Photoemission Extended Fine Structure (ARPEFS) from ordered surfaces. The zero-order problem of photoabsorption in the solid is treated first, followed by a scattering problem which incorporates the scattering ion-cores in a perturbation series (cluster expansion). The dynamics of core-hole relaxation are discussed, but the dynamical effects are shown to be small. The Taylor-series magnetic quantum number expansion is used for the curved-wave, multiple-scattering equations. We argue that a velocity-dependent surface barrier gives primarily an inner potential shift, with no clear evidence for surface electron refraction. Analytic formulas for aperture integration are derived and thermal averaging in a correlated Debye model is extended to multiple scattering. Reasonable values for non-structural parameters in the theory are shown to give very good simulations of the experimental ARPEFS measurements from c(2X2)S/Ni(001) in contrast to previous theoretical calculations. We find, in agreement with full multiple-scattering calculations, that forward focussing is a fundamental feature of ARPEFS and that curved-wave corrections are essential for

quantitative results. Since the scattering path-length difference is
not appreciably altered by forward scattering, the ARPEFS oscillation
frequency is equal to the geometrical path length difference plus a
small potential phase shift, but the amplitude and constant phase of the
oscillations cannot be predicted by theories based upon single-
scattering or plane-wave approximations.

I. INTRODUCTION

Much of the interest in adsorption studies on clean, single-crystal surfaces is based on the usefulness of these systems as well characterized models for more complicated interfaces. Unfortunately, characterization of even these model systems has proved difficult. We have been exploring[1,2] a new approach to determining surface structures using core-level, angle-resolved photoemission. Core-level photoemission provides an element-specific, surface-sensitive, localized probe for adsorbates. By performing angle-resolved measurements with polarized light we may independently orient the emission and polarization vectors: we can view the surface structure from many different angles and emphasize different atoms. These distinctive features of core-level, angle-resolved photoemission have led to a number of experimental measurements and theoretical analysis[3,4] of surface structures, primarily by means of two measurement techniques, azimuthal photoelectron diffraction (APD) and normal photoelectron diffraction (NPD). Recently, we reported[1] the first structure determination using a new photoelectron diffraction technique which we call angle-resolved photoemission extended fine structure (ARPEFS). In this paper we describe a theoretical model which provides the basis for analyzing ARPEFS measurements to extract surface structure information.

Experimental measurements of ARPEFS are very similar to those of normal photoelectron diffraction.[5] An ordered overlayer, adsorbed onto a single crystal, is irradiated with soft x-rays from a tunable, monochromatic photon source. The photon energy is typically scanned from 50 to 500 eV above some core energy level characteristic of the

overlayer. At each energy, the photoemission intensity in a selected emission direction is recorded. The resulting curve of photoemission intensity versus electron kinetic energy contains oscillations which we call ARPEFS. These measurements differ from NPD measurements only in their higher and wider energy range and in the unrestricted choice of emission angles.

The more significant differences between NPD and ARPEFS lie in the interpretation of the measurements, specifically, in the process of extracting the surface structure information. NPD was viewed as being closely related to low energy electron diffraction (LEED); the measured oscillations were ascribed to multiple scattering interferences and analyzed by trial-and-error comparison to sophisticated calculations.[4] ARPEFS, on the other hand, is viewed as closely related to extended x-ray absorption fine structure (EXAFS); the scattering interferences seem to be directly related to individual scattering atoms and the scattering geometry may be extracted using Fourier analysis.[1] One important goal in this paper is to examine the justifications for this simplified view of ARPEFS.

The physical explanation for ARPEFS is based on elastic electron scattering. Core-level photoabsorption gives a localized, atomic-like outgoing photoelectron wave. Direct propagation of this wave into the detector gives the overall atomic-like cross section to the ARPEFS curve. Propagation of this wave to the core region of nearby atoms creates a second set of elastically scattered waves which can also reach the detector. Interference between these two sets of waves gives rise to the ARPEFS. Since the interference extrema occur for electron wavenumbers which are integral multiples of π divided by the difference

in path lengths for direct and scattered waves, the path lengths--and hence the geometry--can be determined from the oscillation frequency.

This is the physical picture presented by Lee[6], although he noted that the same physics had been described earlier, and McDonnell[7] et al. had analyzed angular distributions of Auger emission with an equivalent model. Lee drew strong parallels between EXAFS and angle-resolved photoemission, further suggesting that Fourier transformation might be useful in the analysis of angle-resolved photoemission. This localized, single-scattering cluster model was not, however, thought to be adequate for the analysis of normal photoelectron diffraction data.[4,5] Instead, the full multiple scattering analysis used for LEED was adapted to photoemission, first by Leibsch[8] and later and more extensively by Tong and coworkers.[4] The success of this adaptation is evident in a series of surface structure analysis based on this approach.[3,4]

Despite the success of the NPD analysis, the complexity of the theoretical analysis is discouraging. The first step toward a simpler technique came when Hussain, et al.[9] applied Fourier analysis to theoretically generated, wide energy range NPD curves. Hussain et al. were able to relate peaks in the Fourier spectrum to the interplanar spacings of adsorbate and substrate layers. While this would suggest that some simple model would predict the NPD curve, it appeared inconsistent with Lee's model of localized scattering. Lee's model would seem to predict shells of near neighbor distances in the Fourier transform, rather than the interplanar distances observed. Orders and Fadley[10] resolved this dilemma by investigating in detail a single scattering cluster model similar to Lee's. They noticed that the strong peaking of the scattering angular distribution for backscattering in the

intermediate (100-600 eV) energy range would highlight substrate atoms directly below the adsorbate in the NPD normal emission geometry. Thus, the localized EXAFS-like theory could explain the Fourier transform result without resorting to a multiple scattering model.

With the basic form of the localized cluster theory reconciled with the NPD theoretical curves, we measured[1] intermediate energy off-normal photoelectron diffraction data for c(2x2)S/Ni(100) and applied the techniques of EXAFS analysis in an attempt to derive the surface structure. To emphasize the differences between these measurements and their analysis and the NPD measurements, with their multiple scattering analysis, we have called the new technique angle-resolved photoemission extended fine structure (ARPEFS).

The success of Lee's model as a basis for interpreting the ARPEFS to extract structure does not follow from the quantitative accuracy of published numerical calculations with the model. In fact, numerical calculations by Bullock, Fadley, and Orders[11] demonstrate that the basic single-scattering theory reproduced only the barest outlines of the experimental results. In our opinion, the experimental measurements and Fourier transforms indicate that only backscattering atoms and nearest neighbor atoms contribute substantially to the ARPEFS curve. Many other atoms contributed substantially to the theoretical curves of Bullock et al., giving them too much structure and the theoretical Fourier transform far too many peaks. Although Bullock et al. concluded from their calculations that many scattering atoms must be considered when analyzing ARPEFS, we prefer the interpretation that single-scattering theory does not adequately reproduce the experimental measurements.

In this paper we will concentrate solely on the form of the theory. We will assume that the non-structural parameters and the structure itself are well understood from independent sources. Our ultimate goal for the theory is a simulated curve which reproduces the measured data points to within their experimental precision.

Some of the ingredients of this ARPEFS theory have been presented before. Beyond the qualitative analysis of Lee[6] and McDonnell et al.'s early Auger results[7], theories which describe photoelectron scattering in the intermediate energy range have been developed by Fadley and coworkers,[10,11,12,13] Fujikawa,[14] and Tong and coworkers.[4] The models of Fadley and coworkers and of Tong and coworkers are compared to our model in Table 1. The theory presented by Fujikawa[14] is a full spherical-wave, multiple-scattering, cluster method, but it has not to our knowledge been applied as yet to any photoelectron scattering such as we are interested in here, and we will not discuss it further.

Building on earlier work in azimuthal photoelectron diffraction,[13] Orders and Fadley[10] applied a single-scattering cluster model to normal emission ARPEFS. Individual scattering events are sufficiently simple in this formulation that important insights could be gained about the nature of the electron scattering, specifically the connection between scattering anisotropy and interlayer distances. Unfortunately, this model is not adequate for detailed calculations, and its application to ARPEFS by Bullock, Fadley, and Orders[11] served primarily to spur further work. Very recently, Sagurton, Bullock, and Fadley[12] modified this model to include spherical wave scattering and correlated Debye Waller factors, giving somewhat better agreement with experiment.

The theory described by Tong et al.[4] is complementary to that of the Fadley group. Their methods were developed for NPD studies in the low electron energy regime and extended, with some approximations, to intermediate energies. The sophistication of these calculations has limited their use either for simulation of experimental curves or for further understanding of the photoelectron scattering. Nevertheless this model led to two important developments of particular note: i) the aforementioned Fourier transform results of Hussain, et al.[9] providing the link with earlier NPD results and ii) the "quasi-dynamic" multiple scattering method.[4] This latter result is equivalent to our conclusion that multiple scattering serves to focus the single-scattered waves without introducing new path-length differences: the quasi-dynamical calculation includes all single scattering paths plus all forward multiple scattering paths.

Our work falls somewhat between that of the Fadley and Tong groups. In related papers we have already investigated the nature of curved wave corrections to the single scattering of photoelectrons[15] and derived[16] new approximate formulae for the multiple scattering of spherical waves by a method which we will refer to here as the Taylor series magnetic quantum number expansion (TS-MQNE). Our most significant contribution to the theory of ARPEFS will then be the application of the TS-MQNE multiple scattering equations and the qualitative insight[15] to arrive at a complete but parsimonious account of the elastic scattering of photoelectrons. Thus we include the multiple-forward scattering events (up to fourth order) considered by Tong's curved wave, quasi-dynamic theory, but we retain the relative simplicity of the cluster approach. To treat inelastic damping, we adopt isotropic mean free path damping

from EXAFS work. We include the correlated Debye Waller vibrational correction extended to multiple scattering and we derive an analytic formula for the angle integration effect.

Section II describes the goals of the theory and the division of the ARPEFS problem into a zeroth order problem--discussed in Section IV-- and a scattering problem--discussed in Section V. The effect of the surface barrier is treated in Section VI. A new formula for analytic aperture integration is given in Section VI and thermal averaging is discussed in Section VII. The full theory is compared to experiment in Section VIII, and the importance of each aspect of the theory is discussed.

II. GOALS OF THE THEORY; THE MODEL SYSTEMS

We begin by posing the theoretical problem to be solved. We will use as our example the S(1s) ARPEFS from c(2x2)S/Ni(100) measured along [110] and [001] directions as reported previously[1,2] and analyzed in detail elsewhere.[17] The experimental angle-resolved photoemission partial intensities, I(E), can be reduced to the proportional cross-section oscillations:

$$\chi(E,\hat{R},\hat{\varepsilon}) = \frac{I(E) - I_0(E)}{I_0(E)} \qquad (1)$$

where E is the measured photoelectron kinetic energy. The unit vector $\hat{R}$ specifies the direction to the photoemission analyzer and $\hat{\varepsilon}$ gives the polarization vector orientation. The curve I(E) has been corrected for such effects as photon flux; $I_0(E)$ is taken as the smooth, slowly varying part of I(E). This form is relatively insensitive to errors due to experimental efficiencies, which tend to be cancelled by $I_0(E)$.

Similarly if the theory is asked only to reproduce $\chi(E,\hat{R},\hat{\varepsilon})$, we can concentrate on only the rapidly varying portion of the partial cross section. Specifically we may ignore various constants, density of states, and--at least for S(1s)--any atomic cross-section dependence on energy. To simulate the measurement, then, we must calculate the probability that an electron will enter our angle-resolving aperture, Ω, on irradiating the sample with photons of energy 100-600 eV above the S(1s) absorption edge. Thus we need the continuum orbital, $\psi(\vec{r})$, from a stationary state of the light-plus-sample system. The complete calculation of ψ is a complex problem, primarily because photoabsorption is a dynamic process. Our procedure--implicit in previous work--is to

divide the complete problem into two parts. The first part which we
will call the zeroth-order problem, contains all of the dynamical (time-
dependent) physics; the second part, the scattering problem, includes
the scattering from ion cores as a perturbation on the zeroth-order wave
function. Thus $\psi(\vec{r})$ is constructed in the scattering problem as

$$\psi(\vec{r}) = \psi_0(\vec{r}) + \psi_1(\vec{r}) + \psi_2(\vec{r}) + \cdots \qquad (2)$$

using $\psi_0(\vec{r})$ from the zeroth-order problem, and we form

$$\hat{\chi}(E,\hat{R},\hat{\epsilon}) = \frac{\int_\alpha \psi^*(\hat{R})\psi(\hat{R})\ d\Omega}{\int_\alpha \psi_0^*(\hat{R})\psi_0(\hat{R})\ d\Omega} - 1 \qquad (3)$$

for an aperture of radius α, to compare to the experimental $\chi(E)$ curve.
In the next two sections we define the zeroth-order and scattering
problems and give our solutions to them.

III. The Zeroth-Order Problem

The zeroth-order problem consists of the photoabsorption in the absence of ion-core scattering. To be useful for structure determination, the photoelectron continuum orbital must be representable as a wave about a single center; we are only interested in photoabsorption from localized core level initial state. Thus the zeroth-order problem is nothing more than atomic photoabsorption in the presence of a tenuous medium representing the properties of the material surrounding the photoemitter. We shall want the medium to represent the valence charge density in the metal which is responsible for screening the photo-ion, since screening is a dynamical process. Typically, we would also ask the medium to simulate the interstitial regions of the crystal (between ion cores) smoothly continued over the whole crystal. The only important requirement for the medium is that it present only a very smooth potential incapable of scattering or of attenuating the photoelectron wave anisotropically. For the S/Ni problem we consider a sulfur atom partially embedded in a jellium surface being irradiated by soft x-rays of energy above the S(1s) threshold.

Atomic photoabsorption is well understood[18] and as the jellium surface has only a very small interaction with the S core, we need only summarize the assumptions and conclusions of the photoemission theory. In all practical experimental arrangements for ARPEFS we can assume that the photon beam is a weak, linearly polarized electric field of intermediate energy, 50 eV $<$ hυ $<$ 50 keV. This insures accuracy of the dipole approximation so that we may write

$$\psi_o(\vec{r}) = \langle \vec{r}|\psi_o\rangle\langle\psi_o|\hat{\varepsilon}\cdot\vec{r}|\phi_{1s}\rangle \; \langle\Phi_f|\Phi_o\rangle \qquad (4)$$

where ϕ_{1s} is the (1s) orbital, $\hat{\varepsilon}$ is the polarization (unit) vector of the electric field, Φ_f is the photoion wavefunction and Φ_o is the ground state wavefunction excluding the (1s) orbital.

The angle integration immediately yields the dipole selection rule: expanding $\psi_o(r)$ in spherical harmonics and integrating shows that $\psi_o(\vec{r})$ is a "p" wave:

$$\psi_o(\vec{r}) = Y_{10}(\hat{r})R_{100}(r) \int_0^\infty R_{100}(r)\phi_{1s}(r)r^3 dr <\Phi_f|\Phi_o> \qquad (5)$$

where $R_{100}(r)$ is the radial part of the photoelectron continuum orbital. We emphasize that the angular distribution of the photoelectron in ψ_o is solely determined by the dipole selection rule.

The remaining problem would seem to be a difficult one. Fortunately, the details of the radial wavefunction are almost without consequence for the purpose of determining surface structures. The interference leading to ARPEFS does not depend upon the absolute phase of the photoelectron wavefunction, and we specifically avoid studying slowly varying fine structure so that we may ignore the photoabsorption cross-section structure. Thus if we select a sphere surrounding the photoabsorbing atom within which the potential experienced by the photoelectron is spherically symmetric, e.g., the "core" region, then the phase and amplitude of $\psi_o(\vec{r})$ may be set to arbitrary constants on the surface of the sphere. With no more error than is already introduced in the muffin-tin form of our scattering problem we may extend the radius of this sphere, r_a, to include the entire atomic volume of the photoabsorbing atom.

The form of the photoelectron wavefunction outside r_a will depend on the extent of the dynamic core-hole screening. Noguera et al.[19] have considered the semiclassical problem of the response of a jellium metal to a suddenly created core hole. These authors argue that the screening time is a fraction of the plasmon period, $0.15\ (2\pi/\omega_p)$ for plasmon frequency ω_p. They calculate the photoelectron position classically with $r=vt$: the screening time is ~ 0.04 femtosec in metals, and electrons with energy of a few hundred electron volts have velocities of ~ 100Å/femtosec. Thus we can expect the wavefunction from r_a to $r \sim 4.0$Å to correspond to a partially screened potential. We will, however, take the approximation that the core-hole potential is fully screened at r_a. We expect little error from this choice even though the nearest neighbor scattering atoms lie between r_a and $r \sim 4.0$Å, since the difference between the scattering properties of the partially and fully screened potential wavefunction will be slight. Then our zero-order wavefunction will be

$$\psi_0(\vec{r}) = A(r_a)e^{-r/2\lambda}ih_1(kr)Y_{10}(\hat{r}), \qquad \text{for } r>r_a \qquad (6)$$

where $ih_1(kr)$ is the spherical Hankel function (free spherical wave) and the damping of the electron amplitude due to excitation of the jellium is modelled with a mean-free path λ. The complex constant, $A(r_a)$, contains transition amplitudes and phase shifts which ultimately cancel when $\chi(E,\hat{R},\hat{\epsilon})$ is formed.

IV. THE SCATTERING PROBLEM

For our scattering problem we use an array of spherically symmetric ion cores, the familiar muffin-tin model for solids. The scattering problem itself has been extensively investigated. While Tong and coworkers[4] have applied the multiple scattering methods of LEED directly to the scattering problem we face, the usual techniques become unmanageable in the higher energy range. We have investigated the difficulty posed by the higher energy range, and we have proposed a new approximate method which we call TS-MQNE: Taylor series-magnetic quantum number expansion.[16] Therefore we will concentrate here only on the form of this approximate method and its application to ARPEFS.

The MQNE may be qualitatively described as follows. The basic ingredients in the scattering problem is a wave source, a scattering potential, and an observation point. The wave source may be the original photoemitting atom, or a scattering atom. The scattering potential is taken to be spherically symmetric. The observation point may be a detector or another scattering potential. The first step in the MQNE is to describe the basic scattering problem in a coordinate system in which the $\hat{z}$ axis lies along the vector between the wave source and the scattering potential. Thus we decompose the source wave into partial waves of orbital and magnetic angular momenta quantized along the internuclear axis between source and scattering atoms. If the source wave is originally described in terms of partial waves about a different axis, then this step introduces rotation matrices for the spherical harmonics.

The second step of the MQNE procedure translates the source partial waves to the scattering potential. This translation conserves the magnetic quantum number--the first of two reasons we choose the

internuclear axis for the quantization axis. The third step of the MQNE procedure generates the outgoing scattered wave by multiplying each individual incoming partial wave by a complex scattering matrix element. Our convenient choice of the internuclear separation as the quantization axis now helps a second time: only waves with low magnetic quantum numbers scatter from the potential.[16] The number of waves is directly related to the ratio of the potential radius to the internuclear separation. The restriction of the magnetic quantum number scattered by the potential constitutes the MQNE.

The zeroth-order wavefunction is an $\ell = 1$ spherical wave centered on the photoabsorbing atom. Placing the origin of coordinates on the photoabsorber with the $\hat{z}$ axis along the polarization vector, $\hat{\varepsilon}$, means that this wave is

$$\psi_0(\vec{R}) = \frac{e^{ikR}}{ikR} \cos\theta_{\varepsilon R} \; e^{-L(0)/2\lambda} \tag{7}$$

at our detector, $\vec{R}$. The factor $L(0)$ is the distance in the direction of the detector from the photoemitter to an arbitrary reference plane above the surface. (See Section V). The first-order (single-scattered) wavefunction has spherical waves emanating from every ion core except the photoabsorbing atom:

$$\Psi_1(\vec{R}) = \sum_{a_j \neq 0} \frac{e^{ik|\vec{R}-\vec{a}_j|}}{ik|\vec{R}-\vec{a}_j|} \; \frac{e^{ika_j}}{a_j} \; F(\hat{\varepsilon}, \vec{a}_j, \vec{R}) \; e^{-a_j/2\lambda} \, e^{-L(a_j)/2\lambda} \, . \tag{8}$$

The index j runs over all near by atoms; The vector $\vec{a}$ is the internuclear separation vector between the photoemitter and the first scattering atom. We may expand

$$|R-a_j| \approx R(1 - \frac{a_j}{R}\cos\theta_{a_jR} + \cdots) \approx R - a_j\cos\theta_{a_jR} \qquad (9)$$

to write

$$\frac{e^{ik|\vec{R}-\vec{a}_j|}}{ik|\vec{R}-\vec{a}_j|} \approx \frac{e^{ikR}}{ikR}e^{-ika_j\cos\theta_{a_jR}} \qquad (10)$$

The second and third term in the first order wavefunction accounts for the phase and amplitude of the zero-order wave at the center of the scattering potential at $\vec{a}_j$. The complex number $F(\vec{\epsilon},\vec{a}_j,\vec{R})$ is the scattering factor and it gives the phase and amplitude of the scattered wave in the direction of the detector; its precise nature depends on the scattering approximation chosen. In a plane wave model, $F(\vec{\epsilon},\vec{a}_j,\vec{R})$ would be the scattering factor of atomic physics times $\cos\theta_{\epsilon a}$. The final term in the first order wavefunction is the attenuation of the scattered waves as they propagate from the scattering atom to the reference surface, a distance of $L(\vec{a}_j)$.

Similarly, the double scattered wave is

$$\psi_2(R) = \sum_{b_j\neq 0}\sum_{a_j\neq 0}\frac{e^{ikR}}{ikR}e^{-ika_j\cos\theta_{a_jR}}\frac{e^{ika_j+a_j/2\lambda}}{a_j}$$

$$F(\vec{\epsilon},\vec{a}_j,\vec{b}_j)\,e^{-ikb_j\cos\theta_{b_j R}}\ \frac{e^{ikb_j + b_j/2\lambda}}{b_j}\,F(\vec{a}_j,\vec{b}_j,\vec{R})\,e^{-L(\vec{a}_j+\vec{b}_j)/2\lambda} \qquad .(11)$$

The vector $\vec{b}$ runs between single-scattering and double-scattering atoms. The higher order waves may be written down by analogy.

Interference between the zero-order wave at the detector—which we will call the direct wave—and the single and double scattered waves occurs when the complete wave probability is calculated:

$$\psi(\vec{R})\psi(\vec{R}) = \psi_0^*\psi_0 + (\psi_0^*\psi_1 + \psi_1^*\psi_0) + (\psi_0^*\psi_2 + \psi_2^*\psi_0) + \psi_1^*\psi_1 \qquad (12)$$
$$+ \psi_1^*\psi_2 + \psi_2^*\psi_1) + \cdots$$

The interference leads to ARPEFS when the proportional oscillations are formed.

We detect the photoemission intensity with a small but finite angular acceptance and the scattering atoms vibrate so that every photoelectron scatters from a slightly different system. We must consider this angle integration and thermal averaging before we can hope to simulate the experimental ARPEFS. We have also neglected any effect of the surface on the photoelectron. We take up these topics in the next three sections.

V. REFRACTION AND THE INNER POTENTIAL

The interaction between the fast photoelectron and the conduction electrons of the solid can be approximated as a complex optical potential operating on the photoelectron.[20] The imaginary part of the optical potential serves to attenuate the photoelectron wave; its physical origin is the electronic excitation of the solid plasmon oscillations and electron-hole pairs. We have incorporated this attenuation with the mean free path factors in Section IV. The real part of the optical potential plays no role in scattering; it represents the energy difference between a free electron and that electron screened by the conduction electrons of the solid. When the photoelectron leaves the solid it moves away from the influence of the optical potential. Here we consider the results of this surface barrier.

A photoelectron with energy E within the jellium medium will have energy $E-E_0$ in the vacuum far from the surface. This loss of kinetic energy E_0 may be related to a potential barrier whose total height is V_0, the real part of the optical potential. The height of the barrier determines the energy loss, but the barrier shape will alter the trajectory of the photoelectron. Sagurton et al.[12] adopted a planar step barrier of height V_0 just outside the last row of ion cores. This is the usual first-order model for the surface barrier, introduced for both low energy photoemission[21] and low energy electron diffraction.[20] The important consequence of this model is a prediction that the emerging photoelectron will be refracted in a direction away from the surface normal in the manner of optical refraction with

$$(E)^{1/2} \sin \theta = (E-E_0)^{1/2} \sin(\theta+\Delta\theta) \tag{13}$$

where the angles are measured from the surface normal. Since $E_0 \ll E$ for ARPEFS energies, the angle correction $\Delta\theta$ is small, but it could be significant for high accuracy at larger emergence angles. This correction is, however, not a consequence of the photoemission physics but only results from the particular choice of the potential barrier. As we now discuss, every improvement in the description of the physical barrier serves to reduce this already small correction, to the point that we shall neglect it.

We divide the surface barrier into two parts.[22] The first part is the electrostatic potential of the charge density outside the muffin tin potentials of the surface atoms. This potential is distinctly non-planar, resembling an egg carton on the solid side of the barrier. For a plane wave or a spherical wave whose source point is deep inside the solid, the first-order effect of the electrostatic potential would be optical refraction from the average potential, but the variation of the potential from its average should be about $V_0/2$. More important, a spherical wave originating near the surface barrier will be sensitive to the local geometry of the potential rather than its average. For example, a wave emanating from a surface atom will experience a potential which curves around the surface atom and hence will propagate with little refraction.

The second part of the surface barrier is caused by polarization of the surface electron density (real part) and excitation of surface plasmons (imaginary part). The real part of this potential is long range, corresponding to the image potential if the electron is at rest. The precise form of this potential for a moving electron has not been studied, but we can say that both the shape and size of the potential is

velocity dependent.[23] At low energies the potential has the form of an image potential $V(z) = 1/(z+c)$ depending only on the normal distance, z+c, between the surface and the electron, but saturating when the electron is within a screening length, c. For a fast electron with energy above the plasmon excitation energy, the electron trails a wake of low electron density corresponding to sluggish conduction electrons moving away from the photoelectron charge.[24] As the photoelectron emerges from the surface this screening charge density spreads out on the surface to give the dynamic image potential. A fast electron is already some disance from the center of screening charge: its inner potential is less than that of a slow electron. Furthermore, the surface charge density is slow to redistribute as the fast electron moves away. As a result, rather than an image potential directed along the surface normal, a fast electron works against a force more nearly directed at the spot it emerged from the solid. Such a force does not alter the photoelectron's path.

To summarize, there does not seem to be a strong theoretical basis for extending the optical refraction model into the intermediate energy range as proposed by Sagurton et al.[12] Unfortunately, there seems to be very little experimental evidence on refraction despite its fundamental nature.[25] Until an appropriate theoretical model is treated or experimental measurements are made, we shall use the inner potential shift as the only effect of the surface barrier.

We should note that the inner potential for ARPEFS is the same as that used in LEED[20] but not the same as the E_0 used in EXAFS. The only energy relevant for the scattering problem is the kinetic energy of the electron when it encounters a scattering potential. In ARPEFS and in

LEED the scattered electron is detected, and the inner potential represents the physical kinetic energy lost when the electron travels from the scattering potential edge to the detector. From our previous considerations, this inner potential should be velocity dependent. The conduction electrons are slow to respond to the photoelectron so the positive charge responsible for the dynamic part of the inner potential lies in a wake whose center of gravity lies further away from the photoelectron the higher the energy. Usually, the energy dependence is neglected. In EXAFS, however, the scattered electron is not detected, and the "inner potential", E_0, is a complicated weighted sum of all the photoelectron energies created at a particular x-ray photon energy,[26] and further it is commonly used as an adjustable parameter. Note that in all of these spectroscopies, high precision surface structure determination requires E_0 to be known to within 1 eV, suggesting that further study of the energy dependence of the inner potential would be profitable.

Finally, the imaginary part of the dynamic surface barrier also extends into the vacuum due to excitation of surface plasmons. The corresponding attenuation cancels when the ARPEFS is formed: the direct and scattered waves are equally attenuated. Thus the choice of the "surface" plane at which we discontinue inelastic attenuation is arbitrary as long as it lies above the top layer of ion cores.

VI.   FINITE ANGULAR RESOLUTION

The experimental apparatus for measuring the ARPEFS oscillations has a small but finite angular resolution characterized by half the angle subtended by the aperture at the source, which we call, α. For small apertures, α is the radius of the aperture projected on a unit sphere so that the detected area is $\pi\alpha^2$. The major effect of this finite resolution is to limit the highest observable path-length difference, $p_j = a_j(1-\cos \theta_j)$ such that all paths with $kp_j \gg 1/\alpha$ will be averaged away by the opening, while oscillations corresponding to path-length differences with $kp_j \ll 1/\alpha$ will be individually resolved. With experimental angular resolution of $\pm 3°$, $1/\alpha \sim 10$ and kp will fall between 10 and 100 in practical cases: we have $kp \approx 1/\alpha$. Thus we are in the regime of partial angle averaging, and we must consider the effect in detail. Orders and Fadley[10] previously demonstrated by numerical example that angle-averaging has important effects on the theoretical calculations of azimuthal and energy-dependent photoelectron diffraction. Here we give a simple analytic damping function valid for small apertures and we show that the angle integration preferentially attenuates scattering events with angles near 90°.

If we use $\vec{R}_0$ to denote the position of the aperture center, our angle-averaged intensity is

$$\bar{I} = \int_0^\alpha \sin \theta_{RR_0}\, d\theta_{RR_0} \int_0^{2\pi} d\phi_{xR_0R}\, (\psi_0+\psi_1+\psi_2)^*(\psi_0+\psi_1+\psi_2) \qquad (14)$$

for double scattering. Here θ_{RR_0} is the polar angle between R and R_0 while ϕ_{xR_0R} is the azimuthal angle of R about R_0

We distinguish three terms from the expansion of the squared total wave function i) direct intensity, $\bar{I}_{00}$, ii) scattered-direct intensity, $\bar{I}_{0s}$, and iii) scattered-scattered intensity, $\bar{I}_{ss}$

$$\bar{I} = \bar{I}_{00} + \bar{I}_{0s} + \bar{I}_{ss} \tag{15}$$

where

$$\bar{I}_{00} = \int \psi_0^* \psi_0 \, d\Omega, \tag{16}$$

$$\bar{I}_{0s} = \int \psi_0^*(\psi_1 + \psi_2) + (\psi_1 + \psi_2)^* \psi_0 \, d\Omega, \tag{17}$$

and

$$\bar{I}_{ss} = \int (\psi_1 + \psi_2)^*(\psi_1 + \psi_2) \, d\Omega. \tag{18}$$

Each term contains the coordinates of $\hat{R}$ in the amplitudes of the wavefunction, but the interference terms $\bar{I}_{0s}$ and $\bar{I}_{ss}$ also contain $\hat{R}$ in the wavefunction phase. As the position of $\hat{R}$ moves around the aperture, the wavefunction amplitude always lies near its value at $\hat{R}_0$ and for small apertures we ignore this variation. The phase of the wavefunction is, however, quite sensitive to the position of $\hat{R}$ and even for small apertures this variation should be integrated. The direct intensity integrates to the aperture area times the intensity at R_0:

$$\bar{I}_{00} = \psi_0^*(\hat{R}_0)\psi_0(\hat{R}_0) \, \pi\alpha^2 \tag{19}$$

Each term in the direct-scattered intensity will be of the same form:

$$\bar{I}_{0s}(\vec{a}) = 2\text{Re}[\psi_0^*(\hat{R}_0)\psi_a(\hat{R}_0) \int e^{-ik\vec{a}\cdot(\hat{R}-\hat{R}_0)} d\Omega] \qquad (20)$$

where $\vec{a}$ now represents the bond vector for the scattering event which immediately precedes the trip to the aperture. Expanding $\vec{a}\cdot\hat{R}$ in a coordinate system where $\hat{R}_0$ is the $\hat{z}$ axis gives:

$$-ik\hat{R}\cdot\vec{a} = -ika[\cos\theta_{aR_0}\cos\theta_{RR_0} + \sin\theta_{aR_0}\sin\theta_{RR_0}\cos(\phi_{aR_0R}\phi)],(\Delta\phi) \quad (21)$$

but for small apertures we neglect second-order terms in θ_{RR_0} to write:

$$\bar{I}_{0s}(\vec{a}) = 2\text{Re}\psi_0^*(R_0)\psi_a(R_0)e^{-ika R_0}e^{-ika\cos\theta_{aR_0}}$$

$$* \int_0^\alpha \sin\theta_{RR_0} d\theta_{RR_0} \int_0^{2\pi} e^{-ika\theta_{RR_0}\sin\theta_{aR_0}\cos\phi_{aR_0R}} d\phi. (22)$$

The classical optics problem of Fraunhofer diffraction through a circular aperture leads to the same integration,[27] and we may transfer the result to our problem as:

$$\int_0^\alpha \sin\theta \, d\theta \int_0^{2\pi} d\phi \, e^{-ik\vec{a}\cdot\hat{R}} \approx \pi\alpha^2 [\frac{2J_1(ka\alpha\sin\theta_{aR_0})}{ka\alpha\sin\theta_{aR_0}}] \qquad (23)$$

where $J_1(x)$ is the first order Bessel function.   The factor of $2J_1(x)/x$

is the circular, two-dimensional analog of sin x/x familiar from

diffraction phenomena;[27] its value at x=0 is 1.0, and it falls to zero

at x ≈ 3.8, continuing to higher x with ever smaller oscillations (see

figure 1).   .

By relating the physical parameters to the argument of the aperture

damping function, i.e. $x = \alpha ka \sin \theta_{aR_0}$, we draw the following

conclusions:

i)   backscattering and forward-scattering atoms are not

significantly attenuated by angle integration because sin θ ~

0,

ii)   side-scattering (θ ~ 90°) atoms are maximally attenuated (sin

θ ~ 1).

iii)   the attenuation increases with bond length, radius of the

aperture , and the square root of the energy.

In Fig. 1, we plot the aperture damping function for $\alpha = 3°$ and $\alpha = 10°$.

We also mark the range of ka expected for side-scattering ARPEFS from

nearest neighbor atoms (a = 2.2Å) and more distant atoms (a = 7.5Å).

Both apertures attenuate the more distance atoms; the wider aperture

even damps the nearest neighbor side-scattering atoms.   We further

tentatively conclude that as long as single scattering dominates,

apertures of ≈ 10° would simplify the ARPEFS spectra by eliminating

side-scattering atoms.   Since the larger aperture would decrease the

data collection time by an order of magnitude this conclusion merits

further investigation.   Note that a side-scattered wave which

subsequently forward scatters through a small angle into the detector

will not be attenuated.   The larger aperture will however introduce

higher terms into the phase integral, eqn. (3), and require treatment of the amplitude variation.

Finally, we note that the scattered-scattered intensity may be treated in the same fashion as the direct-scattered term by replacing the last scattering event bond vector, $\vec{a}$ above, by the vector difference in the last scattering bond vectors from the two interfering scattered paths in the scattered-scattered case. In most experimental geometries $|\psi_0| \gg |\psi_s|$ so that we may neglect $\bar{I}_{ss}$ altogether. In these cases, it is convenient for numerical calculations to associate the angle attenuation with the scattered waves so that a single attenuation factor is required for each path rather than a factor for every possible pair of paths.

VII. THERMAL AVERAGING

As the final ingredient in our theory we must allow for the thermally excited vibrational motion of the atoms in the surface. Each atom in the crystal oscillates about some equilibrium position; each photoemission event senses only the instantaneous positions of these atoms. The complete ARPEFS spectrum averages over many photoemission events and hence records an average of the atomic positions according to the probability of each configuration. For typical materials at typical temperatures, the amplitude of these thermal oscillations is not large. However, the effect on the ARPEFS spectrum is significant both in magnitude--thermal averaging is primarily responsible for limiting the highest measurable energy--and in detail--inappropriate thermal averaging can lead to theoretical calculations with far too many scattering events contributing (compare Bullock et al.[11] to Sagurton et el.[12]). Our problem is formally similar to x-ray diffraction where thermal averaging leads to multiplication of diffracted intensity by a Debye-Waller factor $\exp(-2|\vec{K}|^2\sigma^2)$ where $\vec{K}$ is the momentum change in scattering and σ^2 is the mean square displacement projected on $\vec{K}$.[28] Since the momentum change in ARPEFS may be written:

$$\vec{K}_{aR} = k(\hat{R}-\hat{a}) \tag{24}$$

for single scattering off an atom at $\vec{a}$ into a detector at $\vec{R}$, Bullock et al.[11] introduced a factor:

$$e^{-2|\vec{K}_{aR}|^2\sigma^2} = e^{-k^2(1-\cos\theta_{aR})\sigma^2}, \tag{25}$$

where $\cos \theta_{aR} = \hat{a} \cdot \hat{R}$, to include thermal averaging in electron scattering. However, as has been described for the more analogous problem of thermally averaged EXAFS,[29] the form of the x-ray diffraction result is adequate only if the mean square displacements are replaced by the mean square relative displacements. This difference is crucial for electron scattering: the motions of near neighbor atoms are correlated so that the mean square relative displacements of near neighbor is much less than their mean square displacements.

Incorporating the displacement correlations, Sagurton, et al.[12] found some improvement in the agreement between theory and experiment for S(1s) ARPEFS from S/Ni(100) over that reported by Bullock et al. In fact, these authors demonstrate that no thermal averaging at all produces a more reliable result than eqn. (25) with mean square displacements.

The thermal average, like the aperture integration discussed in the previous section, must be performed on the intensity oscillations; we will restrict our attention to experimental geometries which emphasize direct wave interference and ignore the scattered-scattered interference. Furthermore, to avoid obscuring the thermal average with the MQNE notation, we will only consider averaging the zero-order Taylor series term. This is not a serious restriction: the variation in the scattering amplitude over the range of typical vibrational motions is small.

We first consider the single scattering average. The instantaneous position of the scattering atom can be related to the equilibrium

position $\vec{a}_0$, the displacement of the origin (emitting atom), $\vec{u}_0$ and of scattering atom, $\vec{u}_a$ according to

$$\vec{a} = \vec{a}_0 + \vec{u}_a - \vec{u}_0 = \vec{a}_0 + \Delta\vec{u}_a. \tag{26}$$

The vector $\Delta\vec{U}_a$ is the change in the equilibrium bond length. Defining

$$g^{00}(a) = \frac{F(\vec{\epsilon},\vec{a},\vec{R})}{a} e^{-[(a-L(\vec{0}))+L(\vec{a})]/2\lambda}. \tag{27}$$

and noting that the thermal average consists of multiplying by a probability distribution for displacements, and integrating over configurations[28] allows the thermal average (indicated by angle brackets) of the single-scattering direct-wave interference fine structure to be written:

$$\langle\chi_1\rangle = 2\mathrm{Re} \langle g(\vec{a}_0+\Delta\vec{u}_a)e^{ik[|\vec{a}_0+\Delta\vec{u}_a| -(\vec{a}_0+\Delta\vec{u})\cdot\hat{R}]}\rangle. \tag{28}$$

For displacements $|\Delta\vec{u}_a| \ll |\vec{a}_0|$ we can expand

$$|\vec{a}_0 + \Delta\vec{u}_a| \approx a_0 + \hat{a}_0\cdot\Delta\vec{u}_a + \cdots \tag{29}$$

and

$$g(\vec{a}_0 + \Delta\vec{u}_a) \approx g(\vec{a}_0) + \Delta\vec{u}_a\cdot\nabla_a g(\vec{a}_0) + \cdots \tag{30}$$

where forms of order $|\Delta u|^2/a_0^2$ have been dropped. The gradient of $g(\vec{a})$ is similar in size to the curved wavefront corrections described elsewhere.[15] For moderate temperatures and not too soft materials the displacements $\Delta u_{\vec{a}}$ will be small enough so that we can ignore the second term in the expansion of $g(\vec{a})$. Then we have

$$\langle \chi_1 \rangle = 2\mathrm{Re}\ \{ g(\vec{a}_0)e^{ik(a_0 - \hat{\vec{a}}_0 \cdot \hat{R})}\langle e^{-i\vec{K}_{aR} \cdot \Delta\vec{u}_a} \rangle \}. \tag{31}$$

where $\vec{K}_{aR} = k(\hat{R} - \hat{a}_0)$.

The thermal average of the phase term may be derived by following either the x-ray diffraction[28] theory with proper modification or the EXAFS[29] treatment:

$$\langle e^{-i\vec{K} \cdot \Delta\vec{u}_a} \rangle = e^{-\langle(\vec{K} \cdot \Delta\vec{u}_a)^2\rangle/2} = e^{-|\vec{K}|^2\langle(\hat{K} \cdot \Delta\vec{u}_a)^2\rangle/2}. \tag{32}$$

If we identify

$$\sigma_{\vec{a}}^2 = \langle(\hat{K} \cdot \Delta\vec{u}_{\vec{a}})^2\rangle \tag{33}$$

and

$$|\vec{K}|^2 = k^2(2 - 2\cos\theta_{aR}) \tag{34}$$

we retrieve the Debye-Waller form (eqn (25) but $\sigma_{\vec{a}}^2$ becomes the mean square projection of relative displacement (MSPRD) upon the vector $\vec{K}_{aR}$.

To proceed we need to consult some physical model for lattice vibrations which can predict $\sigma^2_{\vec{a}}$. Accurate values may be derived by constructing the normal modes and eigenfrequencies of the solid if the geometry and bonding force constants are known.[28] While potentially useful for theoretical study, this approach requires far too much information for our poorly understood surface system. The Debye model has been adapted to calculate the mean square relative displacements[29,30] in good agreement with experimental EXAFS determinations.[31] Here we need only extend the treatment to include the predicted[32] surface layer dependence and anisotropy of the mean-square displacements that we can expect to encounter and the mass dependence required for an adsorbate. Our result will be a combination of the work of Allan et al.[32] on mean-square displacements on surfaces, of Housley and Hess[33] on mean-square displacements in general, and of Sevillano et al.[30] on mean-square relative displacements.

We expand the MSPRD, $\sigma^2(\vec{0},\vec{a})$ into the sum of the mean-square displacements (MSD) of atoms $\vec{a}$ and of $\vec{0}$ minus twice their displacement correlation function (DCF):

$$\langle [(\vec{u}_a - \vec{u}_0) \cdot \hat{K}]^2 \rangle = \langle (\vec{u}_a \cdot \hat{K})^2 \rangle + \langle (\vec{u}_0 \cdot \hat{K})^2 \rangle \qquad (35)$$

$$-2 \, [\langle (\vec{u}_a \cdot \hat{K})(\vec{u}_0 \cdot \hat{K}) \rangle]$$

To incorporate the directional anisotropy in a simple fashion we approximate

$$\langle (\vec{u}_a \cdot \hat{K})^2 \rangle = \sum_{\alpha=x,y,z} \hat{K}_\alpha^2 \langle (u_{\vec{a}})^2{}_\alpha \rangle. \qquad (36)$$

This relation is exact in the low frequency limit for a medium with isotropic elastic constants[28] or when $\hat{K}$ points along any axis α. We can say that we are calculating $\langle u^2{}_\alpha \rangle$ and approximating the projected mean-square displacement by the indicated weighted average. Denoting[34] the density of modes of frequency ω with $\vec{\alpha}$ direction displacements on atoms in layer ℓ_{3a} by $f_\alpha(\omega, \ell_{3a})$. Then

$$\langle (u_{\vec{a}})^2{}_\alpha \rangle = \frac{\hbar}{2M_a} \int_0^{\omega_{max}} \frac{\coth \hbar\omega/2k_B T}{\omega} f_\alpha(\omega; \ell_{3a}) d\omega \qquad (37)$$

where ω_{max} is the highest frequency of the system. For $[\hbar\omega_{max}/2k_B T] < 3$ (i.e. moderate temperatures) we may apply a modified[35] Thirring expansion[28] of $\coth x \approx 1/x + x/4$ to write

$$\langle (u_a)^2{}_\alpha \rangle = \frac{k_B T}{M_{\vec{a}}} \langle \omega_\alpha^{-2}(\ell_{3a}) \rangle + \frac{\hbar^2}{16 M_{\vec{a}} k_B T} \langle \omega_\alpha^0(\ell_{3a}) \rangle \qquad (38)$$

where the moments of the frequency distribution,

$$\langle \omega_\alpha^n(\ell) \rangle = \int_0^{\omega_{max}} f_\alpha(\omega, \ell) \omega^n d\omega \qquad (39)$$

have been introduced.[34] Since $\langle \omega_\alpha^0(\ell_{3a}) \rangle = 1$ the mean-square displacement in this form requires only one material parameter, the inverse second moment of the frequency distribution.

The corresponding expression for the displacement correlation function between atoms in the same layer will contain moments of the frequency distribution weighted by $\cos \vec{q} \cdot \vec{a}$ where $\vec{q}$ is the wavevector for two dimensional displacements. If we suppose that the moments of the frequency distribution are insensitive to any differences in the density of the modes with the direction of $\vec{q}$, we may replace $\cos \vec{q} \cdot \vec{a}$ by its spherical average[30] $\sin(qa)/qa$.

To proceed we need a model for the frequency distribution. Based on the success reported[31] for EXAFS we adopt the Debye model and set

$$f_\alpha(\omega, \ell_{3a}) = \frac{1}{3} \left\{ \frac{9\omega^2}{[\omega_D(\ell_{3a})]_\alpha^3} \right\} \tag{40}$$

and $q = \omega(q_D/\omega_D)$ where $\hbar\omega_D = k_B\theta_D$, and $q_D = (6\pi^2\rho)^{1/3}$. The Debye temperature θ_D is a material parameter and ρ is the number of atoms per unit volume. Directional, layer dependent Debye temperatures are no more than an expression of the direction and layer dependence of the moments of the frequency distribution:

$$[k_B\theta_D(\alpha, \ell_{3a})]^2 = 3\langle\omega_\alpha^{-2}(\ell_{3a})\rangle^{-2}\hbar^{-2}. \tag{41}$$

Under these conditions we have

$$\langle(u_a)_\alpha^2\rangle = \frac{3\hbar^2}{k_B\theta_D(\alpha, \ell_{3a})M_a} \left[\frac{T}{\theta_D(\alpha, \ell_{3a})} + \frac{\theta_D(\alpha, \ell_{3a})}{48T}\right] \tag{42}$$

and, if atoms $\vec{a}$ and $\vec{0}$ are in the same layer,

$$\gamma_\alpha(0,a) = \langle (u_0)_\alpha (u_a)_\alpha \rangle = \frac{3\hbar^2}{(M_a M_0)^{1/2}} \frac{1}{k_B \theta_D(\alpha,\ell_{3a})} \qquad (43)$$

$$*\left\{ \frac{T}{\theta_D(\alpha,\ell_{3a})} \frac{Si(q_D a)}{q_D a} + \frac{\theta_D(\alpha,\ell_{3a})}{16T} \left[\frac{\sin q_D a - q_D a \cos q_D a}{(q_D a)^3} \right] \right\} \qquad (44)$$

where

$$Si(q_D a) = \int_0^{q_D a} \frac{\sin x}{x} \, dx \approx \frac{\pi}{2} - \frac{\cos q_D a}{q_D a} - \frac{\sin q_D a}{(q_D a)^2}. \qquad (45)$$

The sine integral may be calculated with a numerical form, but the asymptotic form is accurate to 1% for even the smallest $q_D a$ of physical interest, except a = 0 where of course the DCF must cancel the MSD. For atoms in separate layers we know no better than to average the Debye temperatures.

We can also get low temperature limit formulae which overlap the high temperature forms near $T \approx 0.2\theta_D$:

$$\langle (u_a)_\alpha^2 \rangle = \frac{3\hbar^2}{M_{\vec{a}} k_B \theta_D(\alpha,\ell_{3a})} \left[\frac{1}{4} + \frac{T^2}{[\theta_D(\alpha,\ell_{3a})]^2} \frac{\pi^2}{6} \right] \qquad T < 0.2\theta_D \quad (46)$$

and

$$\gamma_\alpha(\vec{0},\vec{a}) = \frac{3\hbar^2}{(M_{\vec{0}} M_{\vec{a}})^{1/2} k_B \theta_D(\alpha,\ell_{3a})} \left[\frac{\pi T \coth[\frac{\pi T q_D a}{\theta_D(\alpha,\ell_{3a})}]}{2q_D a \theta_D(\alpha,\ell_{3a})} - \frac{1}{2(q_D a)^2} \right] \qquad (47)$$

The first result is standard, and the second may be proven by expanding

cotangent in a power series and integrating terms. Taken together these

two limits are adequate to represent the correlated Debye model as

illustrated by comparison to numerical integrations in Fig. 2.

To summarize our results then we write

$$\sigma_{\vec{a}}^2 = \sum_{\alpha=x,y,z} \hat{K}_{\alpha}^2 [\langle (u_{\vec{a}})_{\alpha}^2 \rangle + \langle (u_{\vec{0}})_{\alpha}^2 \rangle - 2\gamma_{\alpha}(\vec{a},\vec{0})] \qquad (48)$$

where $\langle (u_{\vec{a}})_{\alpha}^2 \rangle$ is given by eqn. (42) or (46) and $\gamma_{\alpha}(\vec{a},\vec{0})$ by eqn.(43) or

(47). Each layer is characterized by three directional Debye

temperatures, $\theta_{n,\alpha}$. The studies by Allen and deWette and by Clark et

al.[32] may be used to reduce the number of free parameters. From the

first work we may connect the Debye temperatures in the three crystal

directions to reproduce the ratios of mean-square displacements for the

theoretical crystals of Allen and deWette. From the second work, we may

cause the difference between surface layer and bulk Debye temperatures,

which we may assume to be known, to decay such that the mean-square

displacements approach the bulk values exponentially in three or four

layers.

We have accounted for the changes in the vibrational amplitudes due

to the free surface boundary conditions, but both studies cited above

assume all layers have the same mass. Fortunately, Allen, Alldredge,

and deWette[37] have considered just the problem of mass change, and they

have demonstrated that, under quite general conditions, the mean-square

displacement at high temperatures must be independent of mass, while at

lower temperatures,

$$\langle u_\alpha^2 \rangle' = (\frac{M}{M'})^{1/2} \langle u_\alpha^2 \rangle \qquad (49)$$

where $\langle u_\alpha^2 \rangle$ is the surface MSD for a pure crystal of atomic mass M and the primes indicate a hypothetical mass change of the surface layer without change in force constants. Since the mass dependence is smooth with temperature we may incorporate the adsorbate mass dependence by noting that a Debye temperature, written as:

$$\theta_D = \frac{\hbar}{k_B} (\frac{C_D}{M})^{1/2} \qquad (50)$$

where C_D is a non-physical Debye spring constant, will reproduce the high- and low-temperature-limit mass dependence of the mean-square displacements.

For the double scattering term we must average

$$\chi_2(a,b) = \chi_2(\vec{a}_0,\vec{b}_0) \langle e^{i\vec{K}_{aR} \cdot \Delta\vec{u}_{0a}} e^{i\vec{K}_{bR} \cdot \Delta\vec{u}_{ab}} \rangle$$

$$= \chi_2(\vec{a}_0,\vec{b}_0) e^{-\langle [(\vec{K}_{aR} \cdot \Delta\vec{u}_{0a})+(\vec{K}_{bR} \cdot \Delta\vec{u}_{ab})]^2 \rangle /2} \qquad (51)$$

Expanding the thermal average

$$\langle [(\vec{K}_{aR} \cdot \Delta\vec{u}_{0a})+(\vec{K}_{bR} \cdot \Delta\vec{u}_{ab})]^2 \rangle =$$

$$\langle (\vec{K}_{aR} \cdot \Delta\vec{u}_{0a})^2 \rangle + \langle (\vec{K}_{bR} \cdot \Delta\vec{u}_{ab})^2 \rangle + 2\langle (\vec{K}_{aR} \cdot \Delta\vec{u}_{0a})(\vec{K}_{bR} \cdot \Delta\vec{u}_{ab}) \rangle \qquad (52)$$

we see that the first two terms are MSPRD as given for single scattering while the last factor represents higher order correlations:

$$\langle(\vec{K}_{aR}\cdot\Delta\vec{u}_{0a})(\vec{K}_{bR}\cdot\Delta\vec{u}_{ab})\rangle = \langle(\vec{K}_{aR}\cdot\vec{u}_0)(\vec{K}_{bR}\cdot\vec{u}_a)\rangle - \langle(\vec{K}_{aR}\cdot\vec{u}_0)(\vec{K}_{bR}\cdot\vec{u}_b)\rangle$$

$$- \langle(\vec{K}_{aR}\cdot\vec{u}_a)(\vec{K}_{bR}\cdot\vec{u}_a)\rangle + \langle(\vec{K}_{aR}\cdot\vec{u}_a)(\vec{K}_{bR}\cdot\vec{u}_b)\rangle \qquad (53)$$

As before we write these factors as

$$2\langle(\vec{K}_{aR}\cdot\Delta\vec{u}_{0a})(\vec{K}_{bR}\cdot\Delta\vec{u}_{ab})\rangle =$$

$$2\sum_{\alpha=x,y,z}(K_{aR})_\alpha (K_{bR})_\alpha [\gamma_\alpha(\vec{0},\vec{a})-\gamma_\alpha(\vec{0},\vec{b})-\langle(u_a^{\rightarrow})_\alpha^2\rangle+\gamma_\alpha(\vec{a},\vec{b})] \quad (54)$$

We recognize that the Debye model for the correlated motion of surface atoms is physically untenable: a true Debye model describes low frequency modes in an isotropic continuum particularly relevant to low temperatures. Note however that the MSPRD is sensitive only to moments of the vibrational frequency distribution. The averaging property of the moments mitigates the error in the crude Debye model and, in fact, similar EXAFS Debye-Waller-like factors have been found for force-constant, Debye, and Einstein models of the frequency distribution.[30,31]

VIII. APPLICATION TO C(2X2)S/NI(001)

Having constructed a theory of ARPEFS we now present a preliminary assessment of its predictions. Our study cannot be complete without a thorough examination of the non-structural parameters that the theory requires, but we should expect physically reasonable estimates of the parameters to reproduce most of the features of the experimental curves, allowing our current work to guide both experiment and theory toward a conclusion on the practical accuracy of ARPEFS for structure measurements. In this spirit we have applied the theory of the previous sections to recent S(1s) ARPEFS measurements on c(2X2)S/Ni(001).

The nominal structure of c(2X2)S/Ni(001) is illustrated in cross-section in figure 3. Sulfur occupies a four-fold hollow adsorption site with two nearest neighbors in the plane of the figure and two equivalent neighbors above and below the plane of the figure. Two experimental ARPEFS measurements have been made and reported elsewhere.[17] The first, which we will call [011], aligned both emission and polarization vectors with a bulk [011] axis, making an angle of 45° with the surface normal. The second experiment, called [001] here, used normal emission with the polarization vector inclined 30° from normal in a [100] direction. The proportional partial cross-section oscillations, $\chi(E)$, measured in these experiments, are plotted as solid curves in figures 4 and 5. The measured kinetic energies may be converted to wavenumbers given a value for the real part of the inner potential, E_0. Throughout this paper we will use experimental curves $\chi(k)$ obtained with $E_0=10.5$ eV, close to the reported values used elsewhere[37].

A. Choice of Parameters

The non-structural parameters fall into five classes: the scattering potentials, inelastic scattering, aperture integration, thermal averaging, and numerical convergence.

Our scattering potential phase shifts are those of Orders and Fadley,[10] generated by them from muffin-tin potentials. These potentials are real, and we do not account for the ionization of the photoemitting atom.

Our inelastic mean free path is also the value given by Orders and Fadley[10], $\lambda = (0.753k)$, where k is the electron wavevector in $\mathring{A}^{-1}$. This mean free path lies somewhat below the "universal curve" values. We represent the surface as a plane for the calculation of the path length in the solid, and we place this plane through the adsorbed S atoms. Although some guidelines for this choice are available in surface barrier studies[23], any location above the sulfur atoms is equivalent: any attenuation of the scattered waves in the region above the surface plane is cancelled by the attenuation of the direct wave when the proportional oscillations are formed. Thus we use $L(\vec{a}_j) = \vec{a}_j \cdot \hat{Z}/\hat{R} \cdot \hat{Z}$. A more sophisticated shape for the surface barrier is hardly justified if we persist in using an isotropic mean free path.

For the aperture half-angle we will use 3°. The energy dependence of the electron analyzer used in the experimental measurements indicates that the effective opening may be smaller for high kinetic energy but we will assume a constant opening.

We use the reported[38] bulk Debye temperature for Ni of 390°K appropriate for room temperature. We selected the z axis Debye temperature for Ni as if the S atoms were a layer of Ni, adjusting the Debye temperature to give z axis mean square displacement on the surface

equal to twice the bulk value. This gave a Debye temperature of 300°K. Then the sulfur Debye temperature was corrected for the overlayer mass dependence, giving a $\Theta_{D,z}$=405°K. The x and y Debye temperatures for both atomic species was selected as 1.1 times the z axis values, to give mean square displacements about 1.4 times the bulk values.

The size of our scattering cluster is given by comparing the maximum plane wave scattering amplitude for atoms at the edge of the cluster to an amplitude cutoff value and reducing the cutoff value until no significant changes can be seen in the theoretical curves. We have also only calculated path-length differences less than 10.5Å; the measured curves can easily be filtered to match the theoretical range via the Fourier transform. We have included up to quadruple scattering although only in rare instances will four consecutive scattering events have a path-length difference less than 10.5Å. For each scattering event, the Taylor series order, τ, was selected as the lowest integer which satisfied

$$\left(\frac{f_{max}}{2|\vec{a}|}\right)^{\tau} < C \tag{55}$$

where f_{max} is the maximum of the plane-wave amplitude $|f(\theta,k)|$ over the complete energy range for the scattering angle θ, the scattering bond length is $|\vec{a}|$ and C is a constant set to 0.10. By this means, nearest neighbors and forward scattering atoms are given a higher Taylor order than more distant scatterers at more acute angles.

The atomic geometry was refined by minimizing the mean squared difference between experiment curves and theoretical curves as a

function of atomic coordinates. The procedure is described in Ref. 18. It gives a geometry with S 2.19A from all four Ni nearest neighbors ($d_{\perp}$ = 1.30A) and space the Ni first and second layers by 1.84A.

The calculated theoretical curves are compared to the experimental data in Fig. 4 for the [001] experiment and Fig. 5 for the [011] experiment. The theoretical reproduction of the [001] data, Fig. 4, is good: the oscillatory structures of medium frequency are all matched, with some discrepancies in smaller structures. The results for [011], Fig. 5, are not so good, with significant differences occurring at $5A^{-1}$, $7A^{-1}$ and $9A^{-1}$. The features at $7A^{-1}$ and $9A^{-1}$ are sensitive to the number of successive forward scattering events included in the calculation, and we might expect some improvement here if more accurate scattering potentials are used. Nevertheless, the agreement between theory and experiment is good enough to suggest that distinguishing further improvements in the theory will require a quantitative assessment of the experimental reproducibility.

Thus encouraged, we can reexamine the theory to isolate its most significant components, using the [011] geometry as our example. In Fig. 6 we compare the single-scattering curved wave results to the quadruple scattering curve. The single-scattering result has the underlying frequencies correct, of course, because the frequencies are dominated by the geometrical path-length differences and because we find, in agreement with Tong,[4] that the multiple scattering is primarily forward scattering, which focusses the single-scattered waves and shifts their phase without disturbing their frequencies. However the oscillation phase and amplitude cannot be correctly given in the single-scattering theory.

This point deserves further emphasis, as Bullock, Fadley, and Orders[11] have questioned our previous analysis of the [011] experiment,[1] claiming on the basis of single-scattering calculations that many atoms contribute to the ARPEFS curves. Their conclusions are based on comparing relative single-scattering amplitudes, ignoring the focusing effect of forward scattering (as well as the correlation of vibrational motion and the aperture integration). It is important to note that each neglected forward scattering event is comparable in amplitude to the single-scattering events that they do include. In fact, if we compare the expressions for single and double scattering where the second scattering event has a scattering angle near zero, we find identical terms except for an additional factor of the forward scattering amplitude divided by the bond length. Since the forward scattering amplitude is comparable to the bond length for nearest neighbors, single and double scattering are comparable. We can see this graphically in Fig. 7 where the major backscattering event for the [011] experiment is calculated in both single and double scattering. In the [011] geometry, the Ni atom lying directly behind the S photoemitter contributes a large oscillation with a frequency near 4.4A. The curves show that the single-scattering calculation is too low by nearly a factor of two. The single-scattering calculations therefore cannot be relied upon for relative scattering amplitudes.

Figure 7 also shows that the naive analysis we presented in ref 1 is erroneous. The EXAFS-like backtransformation analysis applied in ref. 1 requires the oscillation phase to be known for the E_0 adjustment procedure. Comparing the two curves in Fig. 7 shows that the single backscattering phase is not close to the double scattering wave phase

even though the oscillation frequency is unchanged. The [011] experiment has been re-analyzed to include the forward scattering effects in ref. 17.

The multiple-scattering curved-wave calculations are also compared to multiple-scattering plane-wave results in Fig. 6. It is evident that the curved wave corrections are essential to describe the ARPEFS oscillations. This would seem to contradict the results of Sagurton et al.[12], who report insignificant curved wave corrections to single-scattering calculations. However, the curved wave corrections apparent in Fig. 6 are primarily in the forward scattering direction[16] and hence only appear in the multiple scattering curves, which are absent in the single-scattering treatment of Sagurton et al[12].

We have also calculated the [011] curve with multiple-scattering using the zero-order Taylor series (homogeneous wave) method[16] and compare it to the higher order Taylor result in Fig. 8. The zero-order curve is quite close to the higher order one, but this is partly a consequence of the [011] geometry: no important scattering atoms are near the nodal plane in the photoemission angular distribution or near a Generalized Ramsauer Townsend resonance, the types of scattering events that we have shown require higher order treatment.[15]

Also in Fig. 8 we have simulated the ARPEFS curve for a 10° aperture but including only the first order aperture damping. Although some of the details of the curve will be subject to correction with more accurate aperture averaging, the size of the oscillations is still large, giving considerable weight to the idea that experimental measurement with 10° apertures could be used to determine surface structures. Assuming that a suitable electron analyzer can be

constructed with this large aperture, the reduction in measurement time by an order of magnitude would be of great value to the experimentalist.

Finally, in Fig. 9 we illustrate some of the effects that vibrational averaging models have on the ARPEFS. In the upper panel we have returned to the uncorrelated Debye model of Bullock et al.[11], but adjusting the surface Debye temperature so that the Debye-Waller σ^2 = $0.01 Å^2$ for the nearest neighbor Ni atoms. There are some changes in the details of the curve, but the differences are not profound. In the bottom panel we illustrate an important point: the overall magnitude of the ARPEFS curve connects the physically allowed values of inelastic mean free path to thermal vibration amplitude (assuming that the elastic scattering amplitude is reasonably accurate). If the vibrational amplitude is reduced to that predicted by the surface vibrational frequency[12] in a harmonic oscillator model, $.003 Å^2$, (corresponding to a S "Debye" temperature of 725°K) then the oscillation amplitude will be far too large to agree with experiment and the mean free path must be reduced by 40% as in Fig. 9. Conversely low mean free path will require a stiffer surface vibration. This ambiguity can be removed by fixing the thermal parameters with a temperature dependent ARPEFS study.

Finally, we address the question, do only a small number of identifiable scattering atoms contribute to the ARPEFS signal? We have contended our experimental ARPEFS curves seem always to be consistent with significant scattering from nearest neighbors and backscattering atoms only.[1,2] Bullock et al.[11] and Sagurton et al.[12] have challenged this idea on the basis of single-scattering calculations. We have shown that these calculations are not adequate, and we note that every improvement in the model used by Bullock et al.[11] serves to favor

backscattering and nearest neighbor scattering. Thus, the correlated Debye model gives less vibrational averaging for nearest neighbor, aperture integration dampens contributions from atoms which are not nearby or backscattering, and forward scattering always accompanies backscattering while other angles are not always so favored. We have calculated the ARPEFS curve including only the four nearest neighbor Ni atoms, the four Ni atoms closest to backscattering in the (011) plane lying further away from S than nearest neighbors and the five Ni atoms in the succeeding (011) plane which are also backscattering. In Fig. 10 we compare the resulting curve to the experiment. It seems clear that these atoms determine the essential character of the ARPEFS signal.

IX. CONCLUSION

We have presented a theory for quantitative calculation of the intermediate energy (100-1000eV) photoelectron diffraction oscillations which we call ARPEFS. For a complete theory we would have to reexamine the non-structural parameters, but the present theory should provide an adequate foundation for surface structure work.

We summarize our present approach as follows. The problem is explicitly divided into two parts, a time dependent, semi-classical solid state photoabsorption problem and a stationary, cluster-type muffin-tin-potential scattering problem. This commonly used division allows us to update the treatment of the photoemission dynamics to show that dynamic core hole screening and surface barrier refraction are smaller effects than we can hope to measure at present. The cluster scattering approach gives us close contact to the interpretation of the ARPEFS oscillations in terms of particular scattering atoms while the application of the Taylor series MQNE small-atom approximation allows economical curved-wave multiple scattering calculations with a full partial-wave expansion of the potential even at these higher energies. This solution to the scattering problem facilitates analytic aperture integration and correlated vibrational averaging of the multiple scattering series, both of which we have derived here. We have also given a method for incorporating the surface dependent vibrational anisotropy into a correlated Debye model for mean-square projected relative displacements.

Our work must be compared to that of Tong and co-workers[4] and of Fadley and co-workers.[10,11,12] Tong, et al. have the advantage of complete summation of the multiple scattering series and of closer

contact to surface-chemistry-dependent potential phase shifts via the Xα
multiple-scattering initial state wave functions. Both of these
advantages may be crucial in the low energy regime, but for most common
surface systems and in the intermediate energy range, we should achieve
multiple scattering convergence easily, and the potentials should be
insensitive to mild electronic changes. The cluster approach allows us
to introduce local physical effects such as photoion core potentials and
dynamic core hole screening which do not have two-dimensional
periodicity and thus are more difficult to introduce into LEED-like
theories.

The single-scattering cluster approach of Fadley et al.[10] has the
virtue of simplicity and some pedigogic value. However, the focusing
effect of forward scattering is a fundamental feature of photoelectron
diffraction, and the scattering amplitudes predicted by single
scattering are not adequate to give quantitative agreement with
experiment.

The apparent success of single-scattering theory to interpret the
ARPEFS[1] was part of our original attraction to the measurement of
surface structure by this method, and we must therefore examine the
utility of the technique in light of the complications introduced by
multiple scattering. In the intermediate energy range, multiple
scattering is primarily forward scattering so that the qualitative idea
that the ARPEFS oscillations represent individual scattering atoms is
unchanged if we associate each forward scattering event with the
backscattering event having a similar path length difference. Thus for
the example given in Fig. 8, the single-scattered wave travels from the
photoemitting S to Ni and backscatters into the detector giving a path

length of 4.35Å. The double scattered wave travels from S to Ni and back to S, scattering into the forward direction giving a path length of 4.37Å. These paths are sufficiently close that we may consider the sum of both scattering events to represent the scattering signal from the Ni atom for the purpose of estimating the ARPEFS signal. The presence of forward scattering does affect our procedure for extracting the geometrical path-length difference. For the example in Fig. 8, we may not simply use the Ni backscattering phase shift to derive the geometry from the oscillation frequency, but instead we must perform the two atom scattering calculation to calculate the effect of the potentials on the waves.

ACKNOWLEDGEMENTS

REFERENCES

1. J.J. Barton, C.C. Bahr, Z. Hussain, S.W. Robey, J.G. Tobin, L.E. Klebanoff, and D.A. Shirley, Phys. Rev. Lett. 53, 272 (1983).

2. J.J. Barton, S.W. Robey, C.C. Bahr, and D.A. Shirley, presented at the First International Conference on the Structure of Surfaces, Berkeley, CA., to be published in the Springer Series in Chemical Physics, 1985;   J.J. Barton, C.C. Bahr, Z. Hussain, S.W. Robey, L.E. Klebanoff, and D.A. Shirley, Proceedings for the Brookhaven Conference, Advances in Soft X-ray Science and Technology, S.P.I.E. v. 447, 82 (1984);   J.J. Barton, C.C. Bahr, Z. Hussain, S.W. Robey, L.E. Klebanoff, and D.A. Shirley, J. Vac. Sci. Technol. A2, 847 (1984).

3. D.A. Shirley, CR in Solid State Materials Science 10, 373 (1982).

4. S.Y. Tong, and C.H. Li, in Chemistry and Physics of Solid Surface v. III, ed. R. Vanselow and W. England, CRC Press, (1982), p. 287.

5. S.D.Kevan, Ph.D. Thesis, Univ. of Calif., Berkeley (1980).

6. P.A. Lee, Phys. Rev. B 13, 5261 (1976).

7. L. McDonnell, D.P. Woodruff, and B.W. Holland, Surf.Sci. 51, 249 (1975)

8. A. Liebsch, Phys. Rev. Lett. 32, 1203 (1974).

9. Z. Hussain, D.A. Shirley, C.H. Li, S.Y. Tong, Proc. Natl. Acad. Sci., 78, 5293 (1981).

10. P.J. Orders and C.S. Fadley, Phys. Rev. B 27, 781 (1983).

11. E.L. Bullock, C.S. Fadley, and P.J. Orders, Phys. Rev. B 28, 4867 (1983).

12. M. Sagurton, E.L. Bullock, and C.S. Fadley, Phys. Rev. B 30, 7332 (1984).

13. C.S. Fadley, Prog. Surf. Sci. 16, 275 (1984)

14. T. Fujikawa, J. Elec. Spectro. Rel. Phen. 26, 79 (1982).

15. J.J. Barton and D.A. Shirley, Phys. Rev. B 32, 1892 (1985).

16. J.J. Barton and D.A. Shirley, Phys. Rev. B 32, 1906 (1985).

17. J.J. Barton, C.C. Bahr, S.W. Robey, Z. Hussain, and D.A. Shirley, LBL-20535.

18. H.A. Bethe and R. Jackiw, Intermediate Quantum Mechanics, 2nd edition, W.A. Benjamin, Reading, MA., 1968.

19. C. Noguera, D. Spanjaard, and J. Friedel, J. Phys. F 9, 1189 (1979).

20. J.B. Pendry, Low Energy Electron Diffraction. Academic Press, London, (1974).

21. G.D. Mahan, Phys. Rev. B 2, 4334 (1970).

22. N.D. Lang, in Solid State Physics, ed. F. Seitz, D. Turnbull, and H. Ehreneich (Academic, New York, 1973), v. 28, p225.

23. P.M. Echenique, R.H. Richie, N. Barberan,and J. Inkson, Phys. Rev. B 23, 6486 (1981); R. Ray and G.D. Mahan, Phys. Lett. 42A, 301 (1972).

24. D. Pines, Phys.Rev. 92, 626, (1953).

25. R.S. Williams, P.S. Wehner, J. Stöhr, and D.A. Shirley, Surf. Sci. 75, 215 (1978); T. Miller, A.P. Shapiro, and T.C. Chiang, Phys.Rev. B, 31, 7915 (1985).

26. B.A. Bunker and E.A. Stern, Phys. Rev. B 27, 1017 (1983).

27. M. Born and E. Wolf, Principles of Optics, 4th ed, Pergamon, Oxford,(1970).

28. A.A. Maradudin, E.W. Montroll, and G.H. Weiss, Theory of Lattice Dynamics in the Harmonic Approximation, Academic Press, New York (1983).

29. G. Beni and P.M. Platzman, Phys. Rev. B 14, 1514 (1976).

30. E. Sevillano, H. Meuth, and J.J. Rehr, Phys. Rev. B <u>20</u>, 4908 (1979).

31 W. Bohmer and P. Rabe, J. Phys. C. 12, 2465 (1979); R.B. Greegor and F.W. Lytle, Phys. Rev. B 20, 4902 (1979); G.S. Knapp, H.K. Pan, and J.M. Tranquada, Phys. Rev, B <u>32</u>, 2006 (1985); V.A. Biebesheimer, E.C. Marques, D.R. Sandstrom, F.W. Lytle, and R.B. Greegor, J. Chem. Phys. <u>81</u>, 2599 (1984)

32. R.E. Allen and F. W. de Wette Phys Rev. <u>188,</u> 1320 (1969); B.C. Clark, R. Herman, and R.F. Wallis, Phys. Rev. <u>139</u>, A860 (1962).

33. R.M. Housley and F. Hess, Phys.Rev. <u>146</u>, 517 (1966).

34. R.E. Allen, G.P. Alldredge, and F.W. de Wette, Phys.Rev.B <u>2</u>, 2570 (1970).

35. Y. Morino, K. Kuchitsu, A. Takahashi, and K. Maeda, J. Chem. Phys. <u>21</u>, 1927 (1953).

36. R.E. Allen, G.P. Alldredge, and F.W. de Wette, J. Chem. Phys. <u>54</u>, 2605 (1971).

37. J.E. Demuth and T.N. Rhodin, Surf. Sci.,<u>42</u>, 261, (1974).

38. J.A. Rayne and W.G. Kemp, Phil. Mag. <u>1</u>, 918 (1956).

Table 1.

	Elastic Scattering				Inelastic Corrections		
	Perturbation Order	Wave Fronts	ℓ_{max} [a]	Surface Barrier	Vibrational Motion	Electronic Excitation	Aperture Integration
Fadley, et al.	single	plane	kr_o	planar abrupt	correlated isotropic	isotropic mean-free path	discrete
Tong, et al.	multiple	curved	~10	planar abrupt	uncorrelated isotropic	isotropic mean-free path	none
This Work	quadruple	curved	kr_o	none	correlated	isotropic mean-free path	analytic

[a] Number of terms in partial wave expansion. The value kr_o implies that ℓ_{max} is allowed to increase with wavenumber.

FIGURE CAPTIONS

Figure 1   Aperture attenuation curves for electron analyzer half-angle

openings of 3° and 10°. The independent variable contains

geometry factors from the emission direction dependent part of

the scattering path length difference. For interference

between direct and scattered waves $\vec{\Delta}$ is the bond vector for

the scattering event which immediately precedes detection; for

interference between scattered waves, $\vec{\Delta}$, is the vector

difference between the bond vectors for the interfering paths.

The line aa gives an indication of the k range typical for

nearest neighbors (2.2Å) with $\sin\Theta_\Delta=1.0$; the line bb

corresponds to similar angles but bond lengths of 7.5Å.

Figure 2. Comparison of solutions to Debye model integrals. The mean

square projected relative displacement along the z axis for S

on Ni is plotted versus temperature for two different

correlation distances, r=50Å (upper curves) and r=2.2Å (lower

curves). The z axis Debye temperature for S was 410°K and for

Ni it was 300°K; and arithmetic average Debye temperature was

used for the DCF. The solid curves give results for numerical

integration of the required integrals, dashed-dot curves are

the results from the modified Thirring expansion of ref 35,

and the dashed line is the low temperaure limit form.

Figure 3   Cross-sectional view of a fcc crystal (001) surface showing

the experimental geometry for the [011] experiment. The

angle-resolving detector is along the vector labeled $\bar{e}$ ([011]

direction); the polarization vector is $\hat{\epsilon}$. The geometrical

path length difference is given by the bond distance from S to

55

a scattering Ni atom plus the distance from the Ni atom to the
plane perpendicular to the emission direction and passing
through the S photoemitter.

Figure 4   Numerical simulation (dashed curve) of the [001] experimental
data (solid curve)

Figure 5   Numerical simulation (dashed curve) of the [011] experimental
data (solid curve)

Figure 6   Comparison of numerical simulation curves for S(1s) ARPEFS
from c(2X2)S/Ni(001) along [011]. (a) Multiple scattering,
plane wave theory, (b) multiple scattering, curved wave
theory, (c)single scattering, curved wave theory. All three
curves used identical geometries and non-structural
parameters.

Figure 7   Comparison of ARPEFS single and double scattering for [011]
emission, but only including the scattering from the Ni atom
directly behind the S from the detector. Thin curve, single
backscattering from Ni; Thick curve, single backscattering
from Ni plus forward focusing through S. The actual
scattering angles are 173° for backscattering and 7° for
forward scattering.

Figure 8   As in figure 6 with (a) zero-order Taylor series (homogeneous
wave theory), (b) full theory, (c) full theory with aperture
damping corresponding to 10° half angle.

Figure 9 As in figure 6 with (a) vibrational amplitudes calculated

without correlation of vibrational motion (mean square

displacements instead of mean square projected relative

displacements), (b) full theory, (c)same as (b) with mean free

path of .44k A and a S Debye temperature of $725\,^{\circ}$K for all

three directions.

Figure 10 Numerical simulation (dashed curve) of the [011] ARPEFS data

(solid curve), but including only a very limited number of

scattering atoms, as described in the text.

Aperture Integration

$k\Delta\sin\theta_\Delta$
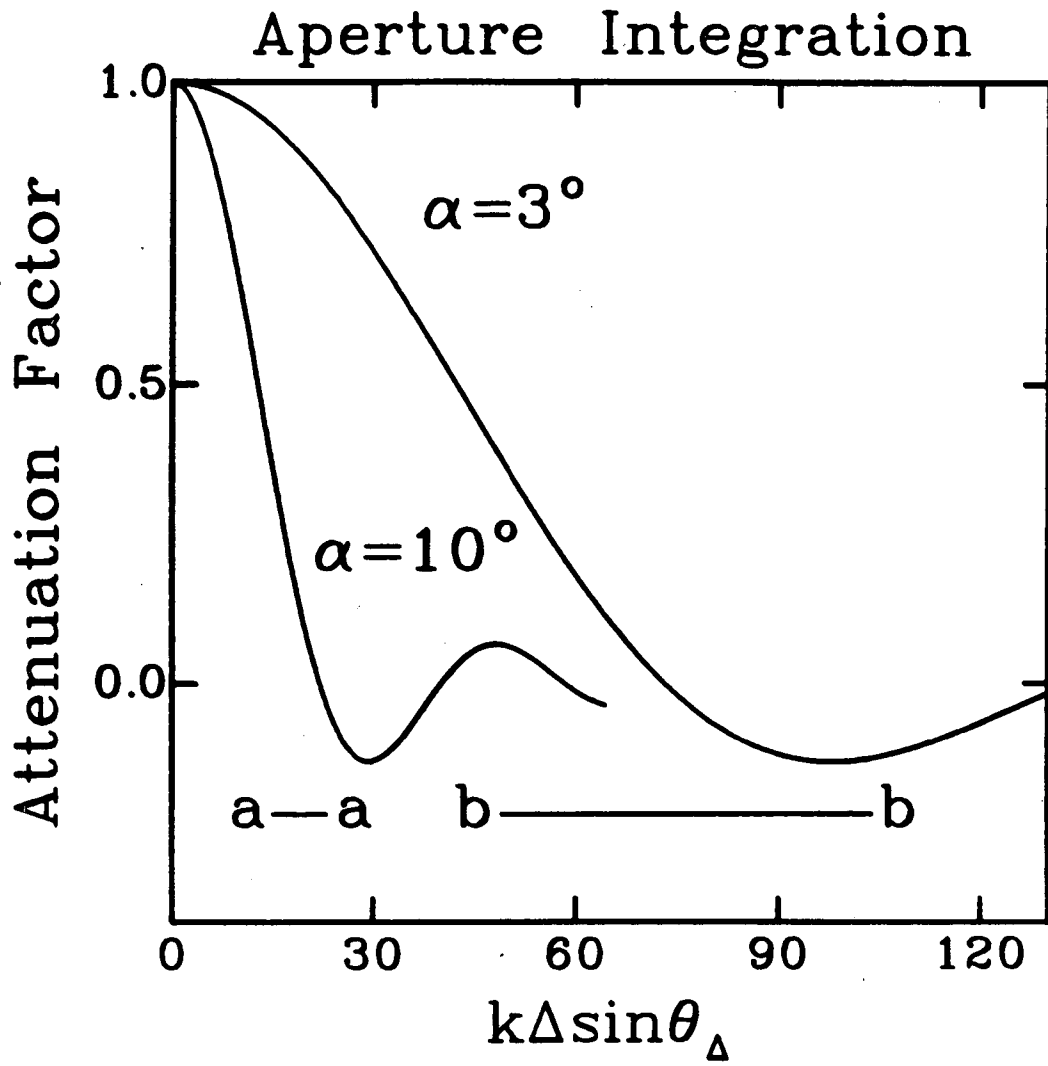
XBL 853-1832

Figure 1

Debye Model MSPRD

Figure 2

59

c(2×2)S/Ni(OOl)

[Oll]

[OIO]

e⁻

S

Ni

θⱼ

1

2

3

3'

4
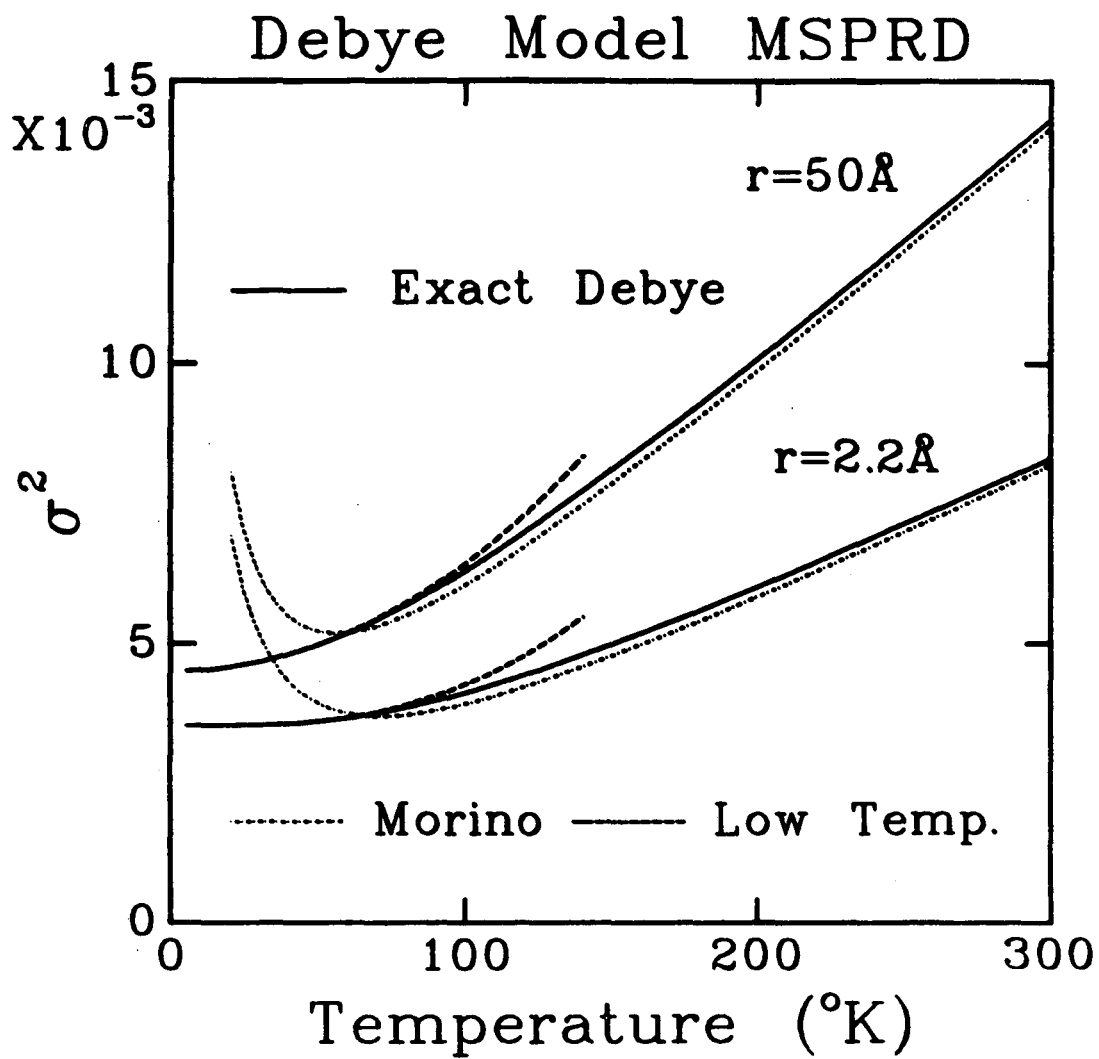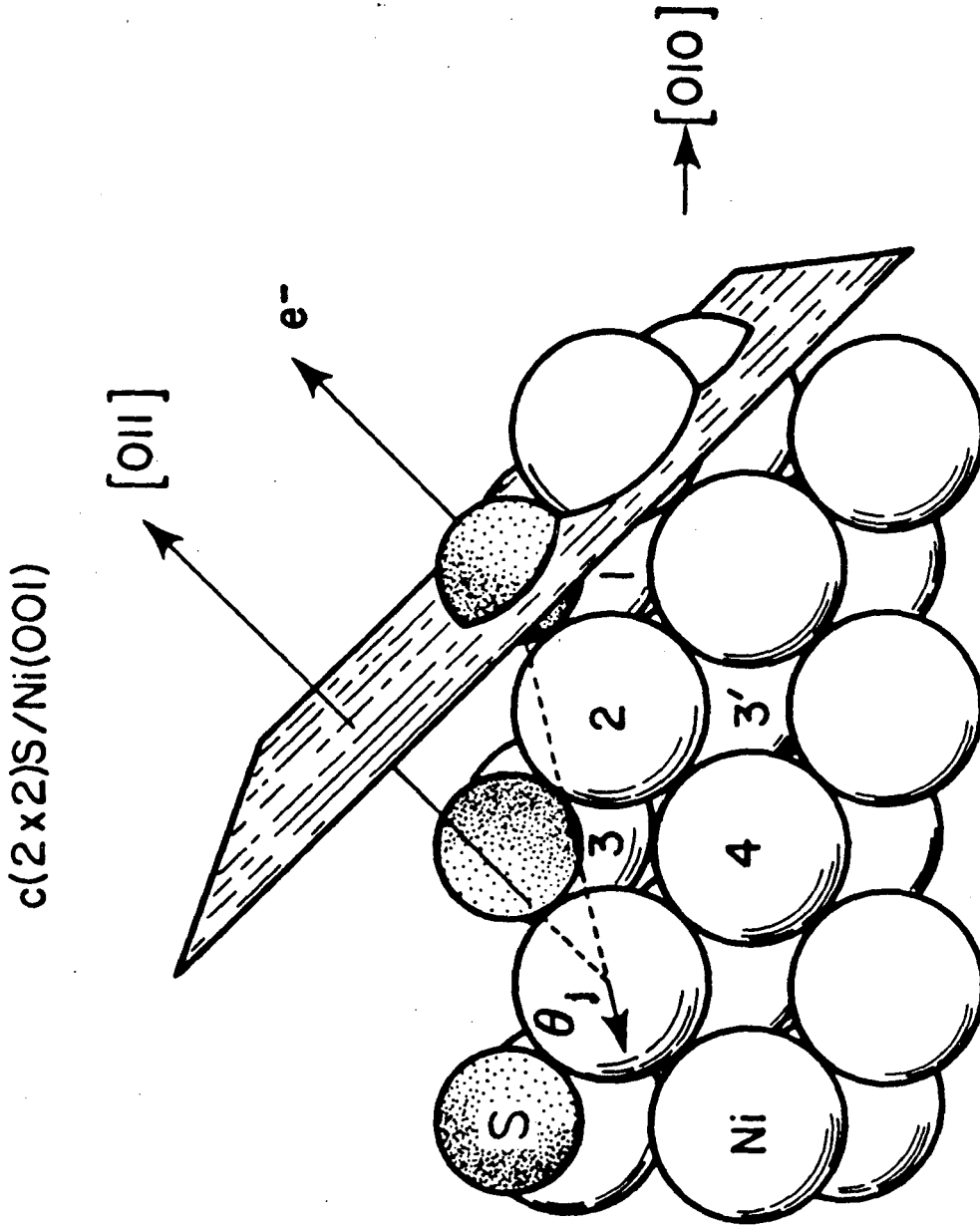
XBL 853-8008

Figure 3

c(2X2)S/Ni(001)−[001]
S−Ni$_1$=1.30Å, Ni$_1$−Ni$_2$=1.84Å
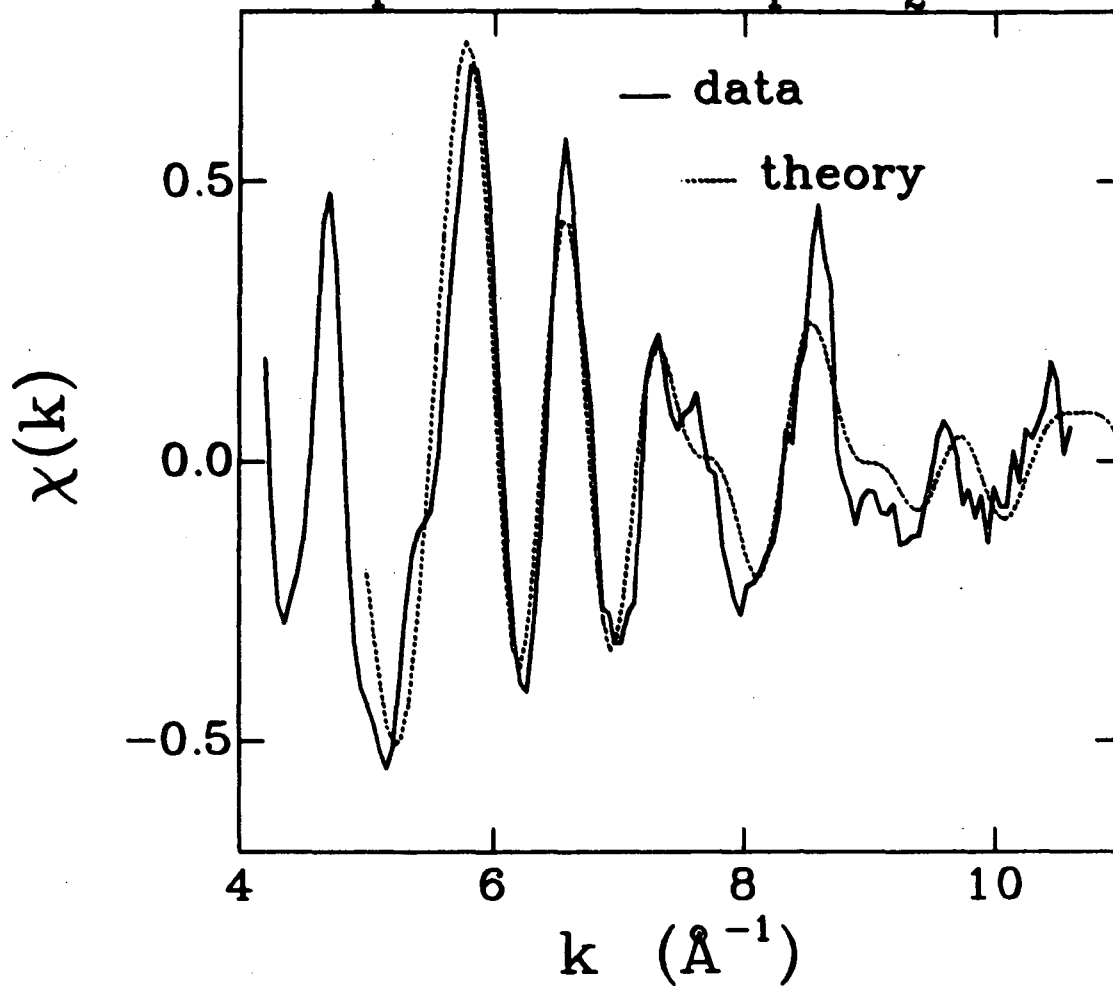
XBL 853-1820

Figure 4

c(2X2)S/Ni(001)−[011]
S−Ni$_1$=1.30Å, Ni$_1$−Ni$_2$=1.84Å

— data
······· theory
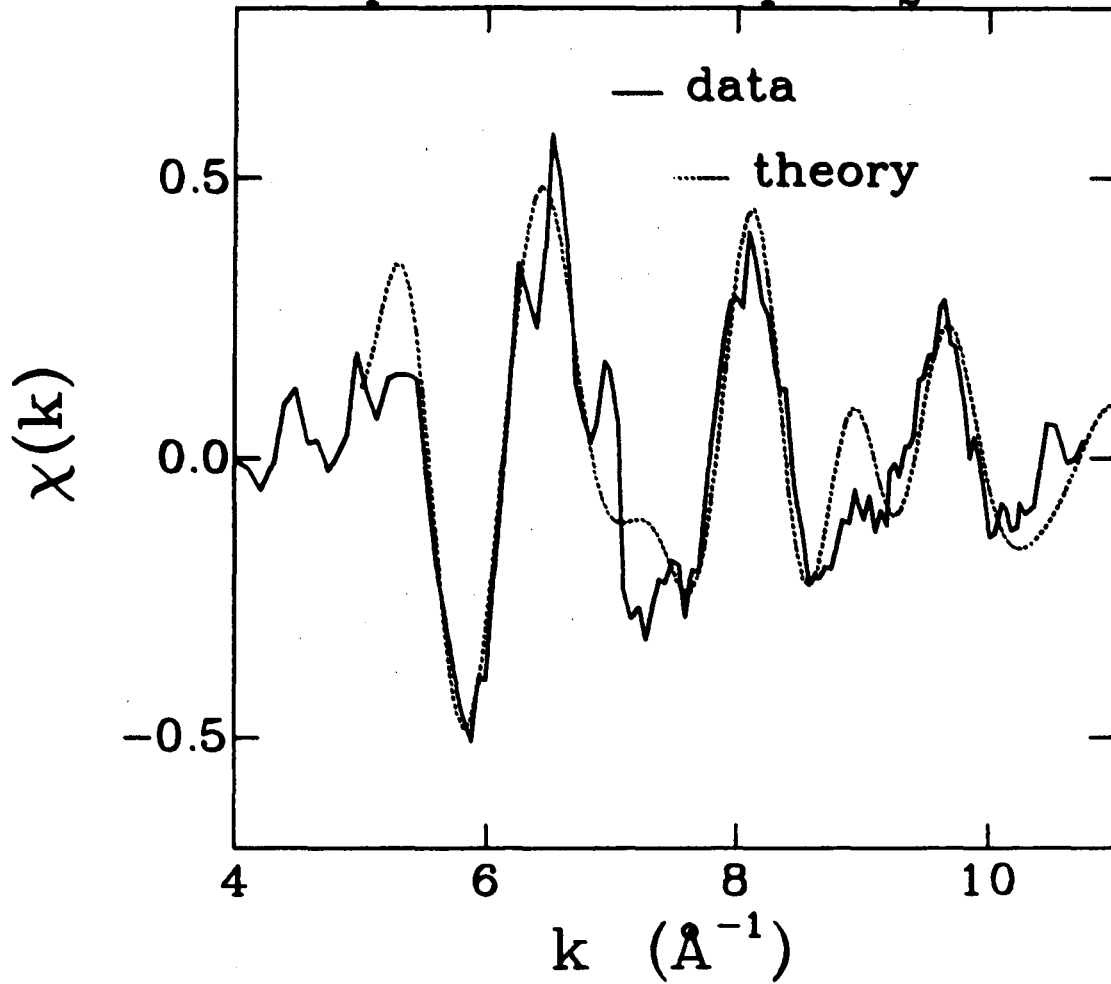
XBL 853-1818

Figure 5

c(2X2)S/Ni(001)

S(1s) — [011]
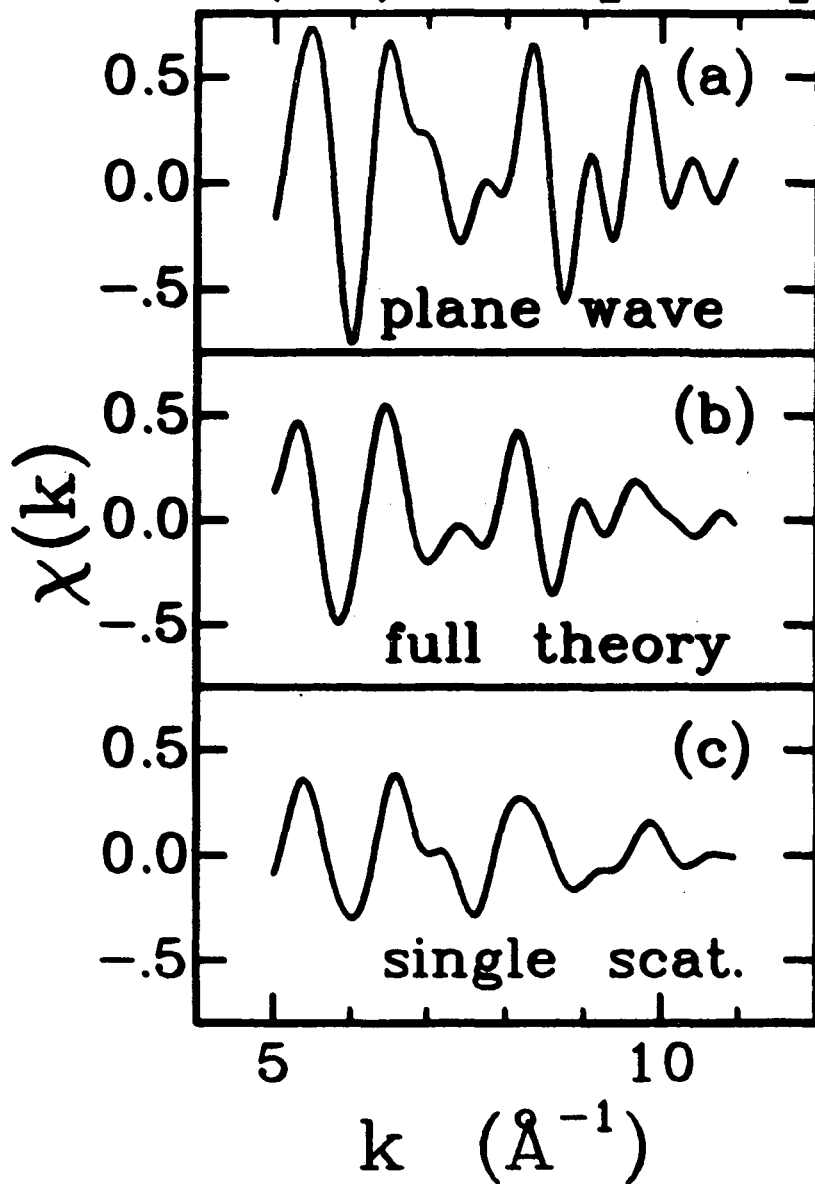
XBL 853-1828

Figure 6

Ni backscatter + S forward scattering
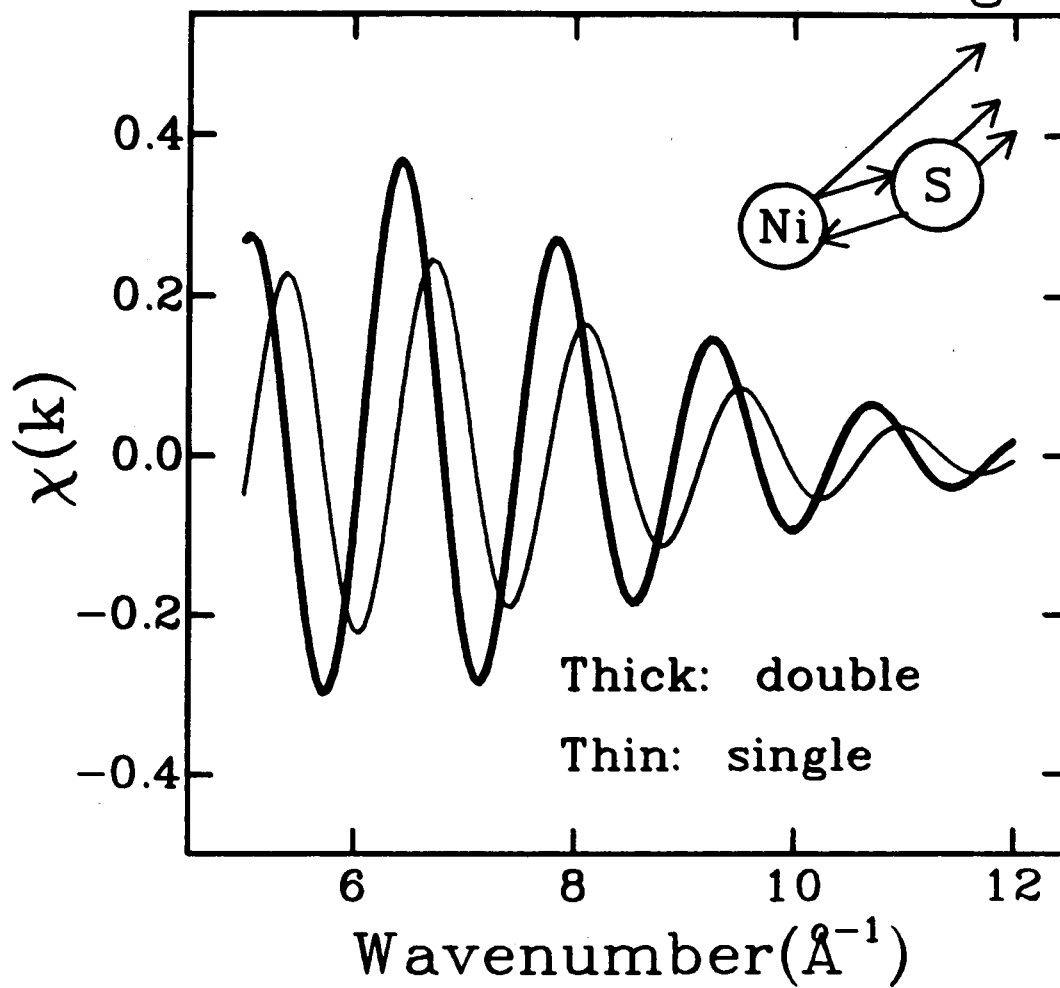
Figure 7

XBL 853-1837

c(2X2)S/Ni(001)
S(1s) – [011]

XBL 853-1831

Figure 8

XBL 853-1829

Figure 9

66

c(2X2)S/Ni(001)-[011]
S-Ni₁=1.30Å, Ni₁-Ni₂=1.84Å

Figure 10

XBL 853-1838